Basement topography and sediment thickness beneath Antarctica's Ross Ice Shelf imaged with airborne magnetic data

Matthew Davis Tankersley[1,1], Huw Joseph Horgan[1,1], Christine Smith Siddoway[2,2], Fabio Caratori Tontini[3,3], and Kirsteen Jane Tinto[4,4]

[1]Victoria University of Wellington
[2]Colorado College
[3]University of Genova
[4]Lamont-Doherty Earth Observatory

November 30, 2022

Abstract

New geophysical data from Antarctica's Ross Embayment illuminate the structure and subglacial geology of subsided continental crust beneath the Ross Ice Shelf. We use airborne magnetic data from the ROSETTA-Ice Project (2015-2019) to locate the basement-cover contact and map the extent of sedimentary basins. We delineate a broad, segmented high with thin (0-500 m) sedimentary cover which trends northward into the Ross Sea's Central High. Before subsiding below sea level, this feature likely facilitated early glaciation in the region and subsequently acted as a pinning point and ice flow divide. Flanking the high are wide basins, up to 3700 m deep, parallel with Ross Sea basins, which likely formed during Cretaceous-Neogene intracontinental extension. NW-SE basins beneath the Siple Coast grounding zone, by contrast, are narrow, deep, and elongate. They suggest tectonic divergence upon active faults that would localize geothermal heat and/or groundwater flow, both important components of the subglacial system.

Basement topography and sediment thickness beneath Antarctica's Ross Ice Shelf

M.D. Tankersley[1,2], H.J. Horgan[1], C.S. Siddoway[3], F. Caratori Tontini[2,4], K.J. Tinto[5]

[1]Antarctic Research Centre, Victoria University of Wellington, Wellington, New Zealand
[2]GNS Science, Lower Hutt, New Zealand
[3]Colorado College, Colorado Springs, CO, USA
[4]University of Genova, Genova, Italy
[5]Lamont-Doherty Earth Observatory, Columbia University, Palisades, NY, USA

Key Points:

- Aeromagnetic analysis reveals basement surface and evidence of fault-controlled extensional basins beneath Antarctica's Ross Ice Shelf
- Active faults at Siple Coast likely influence ice streams through control of geothermal heat, groundwater, and glacioisostatic adjustments
- A basement high beneath Ross Ice Shelf spatially coincides with a lithospheric boundary, with contrasting sedimentary basins on either side

Corresponding author: Matthew Tankersley, matthew.tankersley@vuw.ac.nz

Abstract

New geophysical data from Antarctica's Ross Embayment reveal the structure and subglacial geology of extended continental crust beneath the Ross Ice Shelf. We use airborne magnetic data from the ROSETTA-Ice Project to locate the contact between magnetic basement and overlying sediments. We delineate a broad, segmented basement high with thin (0-500m) non-magnetic sedimentary cover which trends northward into the Ross Sea's Central High. Before subsiding in the Oligocene, this feature likely facilitated early glaciation in the region and subsequently acted as a pinning point and ice flow divide. Flanking the high are wide sedimentary basins, up to 3700m deep, which parallel the Ross Sea basins and likely formed during Cretaceous-Neogene intracontinental extension. NW-SE basins beneath the Siple Coast grounding zone, by contrast, are narrow, deep, and elongate. They suggest tectonic divergence upon active faults that may localize geothermal heat and/or groundwater flow, both important components of the subglacial system.

Plain Language Summary

The bedrock geology of Antarctica's southern Ross Embayment is concealed by 100s to 1000s of meters of sedimentary deposits, seawater, and the floating Ross Ice Shelf. Our research strips away those layers to discover the shape of the consolidated bedrock below, which we refer to as the basement. To do this, we use the contrast between non-magnetic sediments and magnetic basement rocks to map out the depth of the basement surface under the Ross Ice Shelf. Our primary data source is airborne measurements of the variation in Earth's magnetic field across the ice shelf, from flight lines spaced 10-km apart. We use the resulting basement topography to highlight sites of possible influence upon the Antarctic Ice Sheet and to further understand the tectonic history of the region. We discover contrasting basement characteristics on either side of the ice shelf, separated by a N-S trending basement high. The West Antarctic side displays evidence of active faults, which may localize geothermal heat, accommodate movements of the solid earth caused by changes in the size of the Antarctic Ice Sheet, and control the flow of groundwater between the ice base and aquifers. This work addresses critical interactions between ice and the solid earth.

1 Introduction

The southern sector of Ross Embayment beneath the Ross Ice Shelf (RIS; area ~480,000km^2) is poorly resolved because the region is not accessible to conventional seismic or geophysical surveying. Rock exposures on land suggest that RIS crust consists of early Paleozoic post-orogenic sediments, intruded in places by mid-Paleozoic and Cretaceous granitoids (Luyendyk et al., 2003; Goodge, 2020). Since the mid-Cretaceous onset of extension, grabens formed and filled with terrestrial and marine deposits, continuing into the Cenozoic (e.g. Sorlien et al., 2007; Coenen et al., 2019), as the Ross Embayment underwent thermal subsidence (Karner et al., 2005; Wilson & Luyendyk, 2009). The physiography of this region then responded to the onset of glaciation in the Oligocene (Paxman et al., 2019), coinciding with localized extension in the western Ross Sea until 11 Ma (Granot & Dyment, 2018). The Oligocene-early-Miocene paleo-landscape of the Ross Sea sector was revealed by marine seismic data (e.g. Brancolini et al., 1995; Pérez et al., 2021) and drilling that penetrated crystalline basement (DSDP Site 270; Ford & Barrett, 1975) (Figure 3). Recognition of the role of elevated topography in Oligocene formation of the Antarctic Ice Sheet (DeConto & Pollard, 2003; Wilson et al., 2013) and the likely influence of subglacial topography upon ice sheet processes during some climate states (Austermann et al., 2015; Colleoni et al., 2018) motivated our effort to determine basement topography beneath the Ross Ice Shelf.

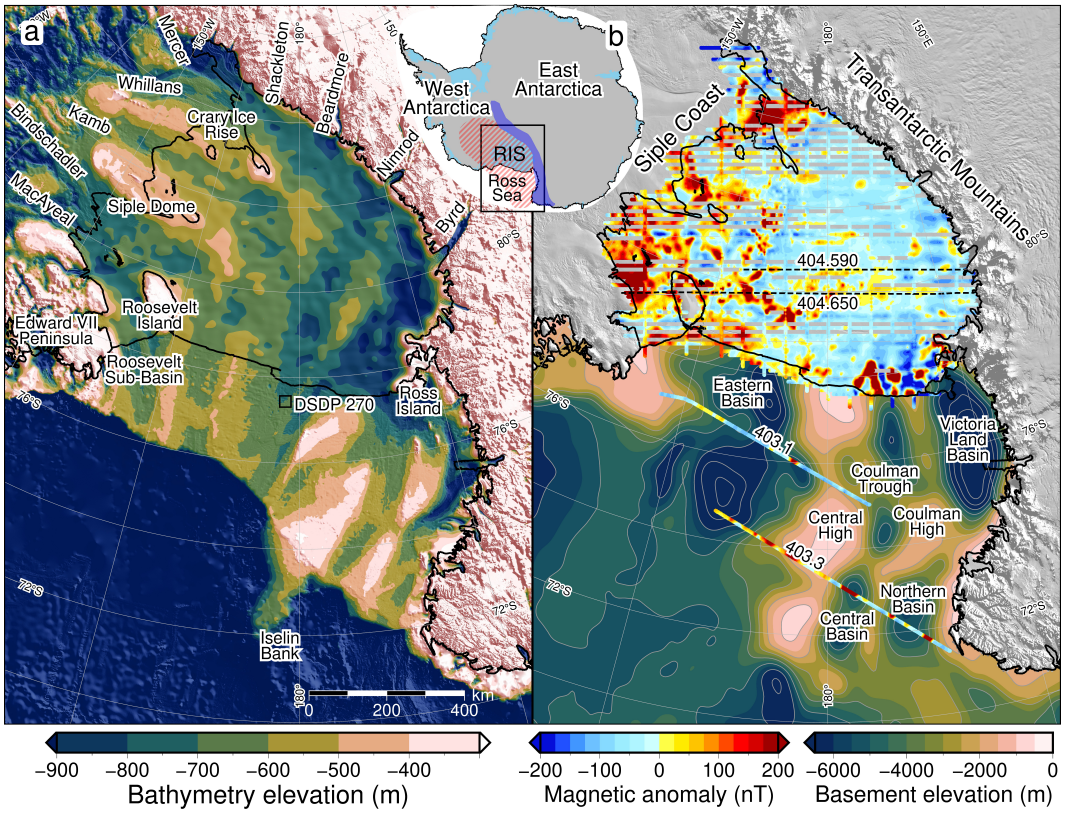

Figure 1. **(a)** Bathymetry and sub-ice bed elevations (Morlighem et al., 2020) including ROSETTA-Ice gravity-derived bathymetry (Tinto et al., 2019) beneath the Ross Ice Shelf (RIS). Labels include ice streams and outlet glaciers. **(b)** Basement depths from ANTOSTRAT marine seismic compilation in the Ross Sea (Brancolini et al., 1995) and airborne magnetic data from ROSETTA-Ice (over RIS) and Operation IceBridge (over Ross Sea). Inset map shows figure location, West Antarctic Rift System (hatched red), and Transantarctic Mountains (dark blue), and ice shelves (light blue). Shelf edge, grounding line, and coastlines in black (Rignot et al., 2013). MODIS imagery from Scambos et al. (2007).

Ice sheet dynamics are of high interest in the RIS region because its grounding zone (GZ) and pinning points (Still et al., 2019) buttress Antarctica's second-largest drainage basin (Tinto et al., 2019). Our work in this sensitive region seeks to delimit the extent and geometry of competent basement because the margins of basement highs are sites of strong contrasts in permeability that influence the circulation of subglacial waters. A spectacular example of the confinement of subglacial water between the ice sheet and basement exists in ice radar profiles for the continental interior (Bell et al., 2011), but the hydrologic system is poorly known for subglacial sediment-filled marine basins that receive terrestrial freshwater influx (Siegert et al., 2018; Gustafson et al., 2021). Possible evidence that basement margins localize geothermal fluids or basinal waters, causing the advection of geothermal heat, comes from elevated values and significant spatial variability of measured geothermal heat flux (GHF) at points around the Ross Embayment (Begeman et al., 2017). Here we present the first map of magnetic basement topography and thickness of overlying non-magnetic sediments for the southern Ross Embayment, developed using ROSETTA-Ice (2015-2019) airborne magnetic data (Figure 1b, Tinto et al., 2019). Our work reveals three major sedimentary basins and a broad basement ridge that separates crust of contrasting basement characteristics.

2 Data and Methods

We applied Werner deconvolution (Werner, 1953) to estimate the depth to the top of the magnetic crust along ROSETTA-Ice flight lines at 10-km spacing (Figures 1b&S4). The approach assumes that sediments and sedimentary rocks produce significantly lower amplitude magnetic anomalies than underlying crystalline basement (Text S6). Here, Werner deconvolution is performed on 2D moving and expanding windows of aeromagnetic line data by isolating anomalies and solving for their source parameters (Birch, 1984). The resulting solutions are non-unique; each observed magnetic anomaly can be solved by bodies at multiple locations and depths by varying the source's magnetic susceptibility and width. The result is a depth scatter of solutions (black dots in Figure 2), which we filtered based on magnetic susceptibility and binned to produce a basement surface (Text S1).

We implemented a 2-step tuning process that ties our RIS magnetic basement to well-constrained seismic basement in the Ross Sea, from the Antarctic Offshore Stratigraphy project (ANTOSTRAT) (Figure 1b, Brancolini et al., 1995). This involved using Operation IceBridge (OIB) airborne magnetic data (Cochran et al., 2014) collected over the RIS and Ross Sea. Minimizing misfits between OIB magnetic basement and ANTOSTRAT basement, as well as between OIB and ROSETTA-Ice magnetic basements, enabled tuning of our method to optimal basement depths (Figures 2, S2, S3e&f, Text S2-3).

Our RIS results (Figure S4) were merged with offshore ANTOSTRAT data (Brancolini et al., 1995) and smoothed with an 80km Gaussian filter to match the characteristic wavelengths of the Ross Sea basement (Text S4). The combined grid (Figure 3a) was then subtracted from bathymetry (Figure 1a, Text S5, Morlighem et al., 2020), to map basins and obtain the sediment thickness distribution for the Ross Embayment (Figure 3b).

We used basement features and geophysical anomaly patterns to infer regional scale faults beneath the RIS. Criteria used to locate faults include 1) high relief on the magnetic basement surface, 2) linear trends that cross zones of shallow basement, 3) high gradient gravity anomalies (Figure S1a) and 4) large contrasts in sediment thickness. Narrow, deep, linear basins are likely to be controlled by active faults (e.g. Finn, 2002; Drenth et al., 2019). We display the inferred faults upon a base map of crustal stretching factors (β-factor; the ratio of crustal thickness before and after extension, Figure 4a), using an initial crustal thickness of 38km (Müller et al., 2007), a continent-wide Moho model (An et al., 2015), and our basement surface as the top of the crust (Text S5).

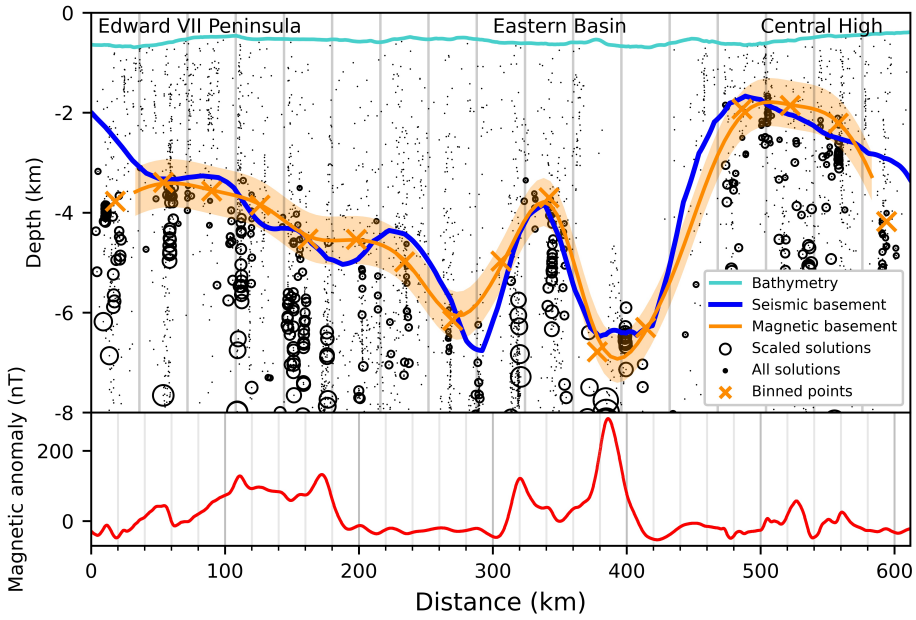

Figure 2. Ross Sea magnetic and seismic basement comparison. Operation IceBridge airborne magnetic data (lower panel) from segment 403-1 (Figure 1b) used in Werner deconvolution to produce magnetic basement (orange line with uncertainty band). Bathymetry from Fretwell et al. (2013). Seismic basement from ANTOSTRAT (Brancolini et al., 1995). See Text S2-S3 for a description of symbols.

3 Results

An almost continuous drape of sediment covers the RIS region (Figure 3b), with only ∼1% of the area having <100m of sedimentary cover. Prominent beneath the midline of the RIS is a broad NNW-SSE trending basement ridge (Figure 3a, Mid-Shelf High; MSH), which comprises most of the shallowest (<700 meters below sea level (mbsl) sub-RIS basement, with several regions having <50m sedimentary cover. Basement is deeper on the East Antarctic side of the MSH, where it averages ∼2400 mbsl, compared to an average depth of ∼1900 mbsl on the West Antarctic side (Figure 3a histogram). Sedimentary fill is ∼400m greater and more uniformly distributed on the East Antarctic side than the West Antarctic side (Figure 3b histogram).

To estimate our uncertainty, we examined the misfit between our basement and ANTOSTRAT and OIB basement (Figures 2, S2, S3e&f, Text S6). There is a median misfit of 480m (22% of average depth) for basement. Incorporating the ∼70m uncertainty in the bathymetry model (Tinto et al., 2019), our sediment thickness uncertainty is 550m (37% of average thickness). A similar 480m basement misfit is estimated by comparing our results to eight active source seismic surveys (Figure 3b, Table S1).

A single broad and deep basin (300 x 600km) separates the MSH and the Transantarctic Mountains (TAM) (Figure 3a, Western Ross Basin). The Western Ross Basin parallels the TAM and has the deepest-observed sub-RIS basement depths of 4500 mbsl, accommodating sediments up to 3800m thick (Figure 3b). It contains a long, narrow NW-SE trending ridge with ∼1500m structural relief above the basement sub-basins on either side. Bordering the MSH on the east, an elongate NW-SE trending basin runs from the RIS calving front to the Siple Coast GZ (Figure 3a), where beneath Siple Dome we discover a 100x200km depocenter reaching basement depths up to 4000 mbsl, with sediments up to 3700m thick. We refer to this depocenter as Siple Dome Basin, a feature bounded on the east by a basement high that trends southward from Roosevelt Island. This high rises to its shallowest point at the GZ, where its sedimentary cover is less than 100m. A second deep, narrow basin (50x200km in dimension) is found along the north margin of Crary Ice Rise, separated from the Siple Dome Basin by a NW-SE ridge underlying Kamb Ice Stream. The basin, labeled Crary Trough in Figure 3a, reaches basement depths of 3200 mbsl, with sediments 1800-2700m thick. The southernmost RIS has an additional depocenter with up to 2000m of fill beneath Whillans Ice Stream (location in Figure 1a).

We inferred the locations of active and inactive sub-RIS faults (Figures 4a & S1). Active faults correspond to narrow, linear basement basins with high-gradient gravity anomalies, prevalent on the West Antarctic side (Figure S1a). Inactive normal and strike-slip faults are inferred along lineaments that segment the shallow MSH into blocks and are oriented parallel to TAM outlet glacier faults. β-factors are indicative of thinned crust and are different on either side of the MSH. The TAM side shows higher β-factors (average 1.99) with low variability. The West Antarctic side has lower β-factors overall (average 1.82), but with some higher values up to 2.1 (Figure 4a).

4 Discussion

Sub-RIS sedimentary basins align with and show lateral continuity with the Ross Sea's Roosevelt Sub-Basin, Eastern Basin, Coulman Trough, and Victoria Land Basin (Figure 3, e.g. Cooper et al., 1995). The MSH passes northward into the Ross Sea's prominent Central High (CH). At the southern RIS margin, the narrow Siple Dome Basin has continuity with the previously identified Trunk D Basin (Figure 3a, Bell et al., 2006). The throughgoing trends imply regional continuity of crustal structure and a common tectonic development of the Ross Sea and RIS regions. Our sediment thicknesses are compatible with those determined by a) eight active-source seismic surveys (Figure 3b), for

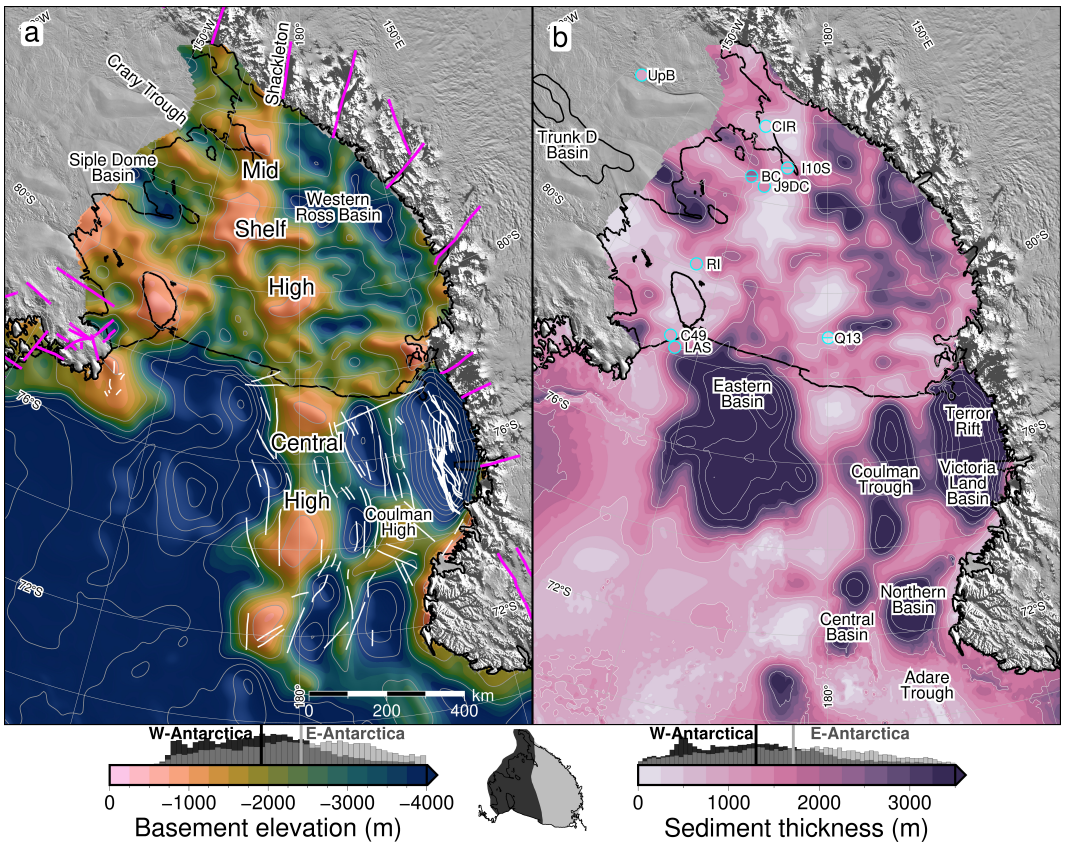

Figure 3. **(a)** Depth to basement (magnetic for Ross Ice Shelf (RIS), seismic elsewhere) contoured at 1km intervals. Pink lines are onshore mapped and inferred faults (Goodge, 2020; Siddoway, 2008; Ferraccioli et al., 2002). White lines are offshore faults (Salvini et al., 1997; Luyendyk et al., 2001; Chiappini et al., 2002; Sauli et al., 2021). **(b)** Sediment thickness contoured at 1km intervals. Previous basement-imaging RIS seismic surveys (Table S1) are plotted on same color scale, with upper and lower uncertainty ranges as circle halves, where reported. Trunk D Basin outlined in West Antarctica (Bell et al., 2006). Color scales for both a) and b) are set to sub-RIS data range. Colorbar histograms show data distribution for East vs West Antarctic sides of the sub-RIS, separated by the Mid-Shelf High. Inset map shows East vs West divide. Vertical lines on histograms denote average values of each side.

which the median misfit is 480m (Table S1), and b) surface wave dispersion indicating 2-4km of sediment under the RIS, similar to our range, with the maximum beneath Crary Ice Rise (Zhou et al., 2022). Three additional western RIS seismic profiles report up to several kilometers of sediment, in general accordance with our results (Stern et al., 1991; ten Brink et al., 1993; Beaudoin et al., 1992). Additionally, machine learning applied to geophysical datasets predicts a high likelihood of sedimentary basins at the locations of Siple Dome Basin and Crary Trough (L. Li et al., 2021).

4.1 West Antarctic Rift System extensional basins

The Western Ross Basin has a configuration similar to the western Ross Sea rift basins (e.g. Salvini et al., 1997) with a broad and deep basin, separated into distinct depocenters by a linear, low relief ridge. The deeper of the depocenters, on the TAM side of the ridge, coincides with a narrow gravity anomaly (Figure S1a). These similarities suggest the sub-RIS continuations of Coulman Trough and Victoria Land Basin (Figure 3b) likely share a common tectonic origin as fault-controlled basins (Figures 3a & 4a) formed through Cretaceous distributed continental extension across the WARS (Jordan et al., 2020). These sub-RIS basins terminate against the southern segment of the MSH (Figure 3a).

The linear ridge within the Western Ross Basin (Figure 3a) may be an expression of normal or oblique faults linked to the southward-narrowing Terror Rift (Sauli et al., 2021), formed due to Cenozoic oceanic spreading in the Adare Trough (Figure 3b, Granot & Dyment, 2018). The Western Ross Basin, with up to 3800m of fill, terminates along the prominent edge of the MSH that lines up with the fault-controlled trough and crustal boundary that passes southward beneath Shackleton Glacier (Borg et al., 1990). We interpret the basement lineament (Figure 4a) as a transfer fault separating sectors of crust extended to different degrees.

The southeastern RIS margin is distinguished by linear ridges and narrow, deep basins. The prominent NW-SE basement trends coincide with high-gradient gravity anomalies (Figure S1a, Tinto et al., 2019) and thick sediments, suggesting normal fault control and active divergent tectonics beneath the GZ. Our Siple Coast cross-section (Figure 4b) displays dramatic basement relief, exceeding 2km, in the Siple Dome Basin and Crary Trough, which we attribute to displacement upon high angle faults. Portions of basin-bounding faults were previously detected by ground-based gravity surveys upon the Whillans Ice Stream flank (Figure 4a, Muto et al., 2013) and site J9DC (Figure 3b), where large variations in sediment thickness indicate up to 600m of fault throw (Greischar et al., 1992). The continuity between the narrow Siple Dome Basin (this study) and the Trunk D Basin (Figure 3a, Bell et al., 2006) suggests that the active tectonic domain continues southward past the GZ. The fault-controlled tectonic basins may be an expression of a crustal response to the lithospheric foundering hypothesized beneath the South Pole region (Shen, Wiens, Stern, et al., 2018).

4.2 Cryosphere-groundwater implications

Fault juxtaposition of low-permeability basement next to permeable basin fill, in a subglacial setting, is likely to affect groundwater reservoir capacity and promote fluid overpressure of the ice sheet-confined aquifer (e.g. Ravier & Buoncristiani, 2018), with consequences for ice sheet processes (Christoffersen et al., 2014). The effects of deep voluminous groundwater within the sub-Whillans fault-controlled basin, discerned using magnetotellurics, are thought to influence ice streaming (Gustafson et al., 2021). Groundwater discharge and recharge along fault damage zones (Jolie et al., 2021) may influence the distribution of heat in the subglacial environment (Burton-Johnson et al., 2020). Modulated by pressure from the overriding ice sheet (Gooch et al., 2016), upward movement and discharge of waters may deliver heat that induces basal melting. Alternatively, basin

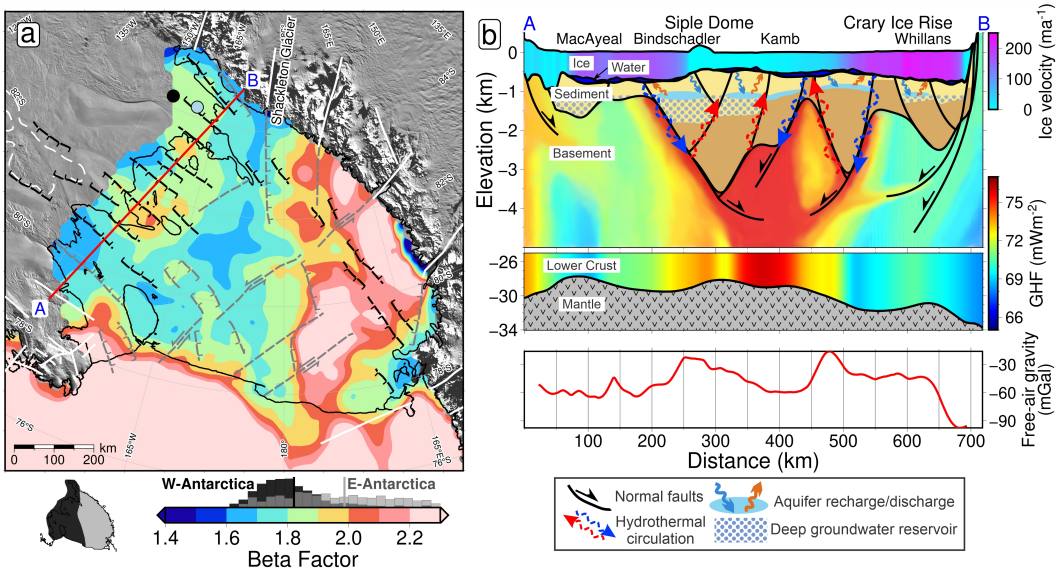

Figure 4. Tectonic interpretation of the sub-Ross Ice Shelf (RIS). **(a)** β stretching factors (Text S5), with sediments removed. Colorbar histogram shows data distribution of West vs. East Antarctic sides, same as Figure 3. Black and grey lines indicate inferred active and inactive faults, respectively, with kinematics shown with half-arrows (strike or oblique-slip) and hachures (normal-sense). White lines show previously reported faults, same as Figure 3a. Dashed-white outline is Trunk D Basin (Bell et al., 2006). Black and blue dots show Subglacial Lake Whillans and sedimentary basin from Gustafson et al. (2021), respectively. Cross-section A-B in red. **(b)** Siple Coast cross-section from A-B, showing basin sediments bounded by faults, with geothermal heat flux (GHF) through the crust (lower panel from Burton-Johnson et al. (2020), upper panel interpreted) with implications for subglacial hydrology. Ice surface, ice base, and bathymetry from Morlighem et al. (2020). Ice streams colored by velocity (Mouginot et al., 2019). Moho is from Shen, Wiens, Anandakrishnan, et al. (2018). Lower panel shows ROSETTA-Ice gravity. Named features are labeled on top.

recharge can sequester heat at lower depths within permeable basin fill. Regionally elevated GHF modeled along the Siple Coast (Shen et al., 2020) and anomalously high GHF (285 mW/m^2) at Subglacial Lake Whillans (Figure 4a, Fisher et al., 2015) are likely the result of the active extensional setting and strong GHF localization upon faults bounding sedimentary basins. If this localization persists beneath the Siple Coast ice streams, it is likely to influence ice flow.

At a more regional scale, active graben-bounding faults likely accommodate relative motion in response to changes in ice sheet volume along the Siple Coast, a region underlain by low-viscosity mantle (Whitehouse et al., 2019; Shen, Wiens, Anandakrishnan, et al., 2018). In this region, Kingslake et al. (2018) found evidence of swift glacioisostatic rebound following Holocene deglaciation, with changes in bed elevation and geometry producing a negative feedback (cf. Lowry et al., 2020; Coulon et al., 2021) that drove ice sheet re-advance and re-stabilized the ice sheet. The matter is receiving considerable debate (Neuhaus et al., 2021).

4.3 Central High - Mid-Shelf High

Using contrasts in crustal characteristics, including magnetic and gravity anomalies, Tinto et al. (2019) identified a mid-Ross Embayment north-south trending geologic boundary separating crust of East and West Antarctic affinity. Geological substantiation comes from basement rock samples recovered from the CH at DSDP 270 (Ford & Barrett, 1975), and at Iselin Bank (Figure 3, Mortimer et al., 2011), which have lithologic affinities to the TAM. The MSH in the magnetic basement coincides with this boundary, as does the Ross Sea's CH, an association that is borne out by passive-seismic studies that show the boundary to be present at lithospheric scale (Cheng et al., 2021; White-Gaynor et al., 2019). The distinct geologic properties on either side of the MSH related to West versus East Antarctic type crust (Tinto et al., 2019) appear to have controlled the respective responses to WARS extension. We determined high and homogeneous β-factors on the TAM-side, indicating distributed crustal extension. The West Antarctic side's β-factors indicate lesser extension, but with specific sites of more extreme thinning (Figure 4a). The greater amount of extension on the East Antarctic side coincides with the deeper bathymetry (Figure 1a), deeper basement, and thicker sediments (Figure 3).

The CH-MSH basement feature trends southward into the TAM, where its western edge aligns with Shackleton Glacier, occupying a major fault separating the distinct geologic domains of the central and southern TAM (Borg et al., 1990; Paulsen et al., 2004). Previous authors noted the alignment of the Shackleton Glacier Fault, a 250-km long fault on the south side of the TAM (Drewry, 1972), and a prominent magnetic lineament at the South Pole (Studinger et al., 2006). This N-S sequence of structures may be an expression of the East Antarctic craton margin or a major intracontinental transform (Figure 4a, Studinger et al., 2006). The spatial correspondence of the East-West Antarctic geologic boundary, the N-S series of linear features, and the prominent basement highs suggest the CH-MSH is a major tectonic feature that, through tectonic inheritance (Corti et al., 2007), has influenced the rift architecture and development of Ross Embayment.

Paleotopographic reconstructions of the early Oligocene depict a proto-Ross Embayment divided by a long, narrow mountain range (the MSH-CH), emergent above sea level (Paxman et al., 2019; Wilson et al., 2012), that hosted alpine glaciers and small ice caps (De Santis et al., 1995). These ice caps represent the initial glacial stage in the region and once established, were the centers from which continental ice expanded to the outer Ross Sea continental shelf (Bart & De Santis, 2012). Between the late Oligocene and mid-Miocene, up to 500m of subsidence and sedimentation occurred (Leckie, 1983; Kulhanek et al., 2019) and the CH became covered in sediment (De Santis et al., 1995). The geophysical similarities and continuity between the Ross Sea's CH and the RIS's MSH

imply a similar glaciation and subsidence history for the RIS region as for the Ross Sea. A terrestrial/alpine stage for the MSH helps to explain the region's potential to hold the late Oligocene's larger-than-modern ice volumes (Wilson et al., 2013; Pekar et al., 2006). Analysis of subglacial sediment identified a major ice flow divide between East and West Antarctic ice since the Last Glacial Maximum (X. Li et al., 2020; Licht et al., 2014; Coenen et al., 2019). These findings highlight the CH-MSH as important features for both Oligocene ice sheet development and the subsequent evolution of the ice sheet and ice shelf, as documented in the Ross Sea (Halberstadt et al., 2016).

4.4 Thermal subsidence and sedimentation

Incorporating the updated basement basin extents and geometries into post-rift thermal subsidence modeling will enable better constrained paleotopographic reconstructions. For the sub-RIS, these reconstructions (Wilson et al., 2012; Paxman et al., 2019) use a post-Eocene subsidence model based on gravity-derived basin geometries and uniform β-factors (Wilson & Luyendyk, 2009). This model predicts uniform stretching of the eastern sub-RIS from the ice front to the Siple Coast, while our β-factors show increasing stretching from the ice front to the Siple Coast. This observed additional thinning likely has resulted in more subsidence for Siple Dome and the north flank of Crary Ice Rise, which can now be accounted for in reconstructions. Our sediment thickness comparison with past models (Text S5, Wilson & Luyendyk, 2009) shows the majority of the sub-RIS, especially the Siple Coast, contains more total sediment than previously estimated (Figure S1f). Depending on the age of this sediment, reconstructions may need to account for the additional sediment deposition and loading.

5 Conclusions

Here we present a depth to magnetic basement map for the Ross Ice Shelf (RIS) from Werner deconvolution of airborne magnetics data. The RIS magnetic basement is tied to Ross Sea seismic basement, providing the first synthetic view of Ross Embayment crustal structure. Subtracting bathymetry, we obtain the sediment thickness distribution and calculate crustal extension factors for the sub-RIS. The extensional features we image, resulting from West Antarctic Rift System extension, have continuity with Ross Sea basement structures to the north, and the prominent Mid-Shelf High trends northward into the Ross Sea's Central High. This combined high separates East and West Antarctic type crust, affected by different degrees of continental extension. The Mid-Shelf High was likely subaerial in the Oligocene, able to support alpine ice caps in early Antarctic glaciation, and subsequently to form an ice flow divide between the East and West Antarctic Ice Sheets. Newly identified narrow, linear, deep sedimentary basins provide evidence of active faults beneath the Siple Coast grounding zone, where thinned crust overlying anomalous mantle (Shen, Wiens, Anandakrishnan, et al., 2018) likely experiences elevated geothermal heat flow promoting the formation of subglacial water. Faults that control basement margins may accommodate motion caused by the glacioisostatic response to ice sheet volume changes. Subglacial sedimentary basins in this setting likely contain confined aquifers with permeable basin fill. Here, ice overburden pressure would control flow both between and within the subglacial and groundwater systems, possibly localizing geothermal heat. Updated sediment thickness and basin extent should be incorporated into new paleotopographic reconstructions of time intervals of interest for paleo-ice sheet modeling. Our work contributes critical information about Ross Embayment basement topography and subglacial boundary conditions that arise from an interplay of geology, tectonics, and glaciation.

6 Open Research

ROSETTA-Ice and OIB magnetics data are available from https://pgg.ldeo.columbia.edu/data. Results from this study are available to download from https://doi.pangaea.de/10.1594/PANGAEA.941238. A Jupyter notebook documenting our workflow is available at https://zenodo.org/badge/latestdoi/470814953.

Acknowledgments

Funding support from the New Zealand Ministry of Business and Innovation and Employment through the Antarctic Science Platform contract (ANTA1801) Antarctic Ice Dynamics Project (ASP-021-01) and the National Science Foundation (1443497 and 1443534). We are grateful to Robin Bell, Isabel Cordero, Alec Lockett, Joel Wilner, Zoe Krauss, and the entire ROSETTA-Ice team for undertaking the ambitious data acquisition and processing effort. We thank Katharina Hochmuth and one anonymous reviewer for thoughtful reviews which greatly improved the manuscript, as well as Chris Sorlien, Tim Stern, Simon Lamb, Lara Pérez, Wei Ji Leong, and Dan Lowry for valuable input. Figures used GMT6/PyGMT (Wessel et al., 2019; Uieda et al., 2021), with a script adapted from Venturelli et al. (2020). Geosoft Oasis Montaj^{TM} was used for magnetics processing and Werner deconvolution.

References

An, M., Wiens, D. A., Zhao, Y., Feng, M., Nyblade, A. A., Kanao, M., ... Lévêque, J.-J. (2015). S-velocity model and inferred Moho topography beneath the Antarctic Plate from Rayleigh waves: Antarctic S-velocities and Moho. *Journal of Geophysical Research: Solid Earth*, *120*(1), 359–383. doi: 10.1002/2014JB011332

Andrews, J. T., & LeMasurier, W. (2021). Resolving the argument about volcanic bedrock under the West Antarctic Ice Sheet and implications for ice sheet stability and sea level change. *Earth and Planetary Science Letters*, *568*, 117035. doi: 10.1016/j.epsl.2021.117035

Austermann, J., Pollard, D., Mitrovica, J. X., Moucha, R., Forte, A. M., DeConto, R. M., ... Raymo, M. E. (2015). The impact of dynamic topography change on Antarctic ice sheet stability during the mid-Pliocene warm period. *Geology*, *43*(10), 927–930. doi: 10.1130/G36988.1

Bart, P., & De Santis, L. (2012). Glacial intensification during the Neogene: A review of seismic stratigraphic evidence from the Ross Sea, Antarctica, continental shelf. *Oceanography*, *25*(3), 166–183. doi: 10.5670/oceanog.2012.92

Beaudoin, B. C., ten Brink, U. S., & Stern, T. A. (1992). Characteristics and processing of seismic data collected on thick, floating ice: Results from the Ross Ice Shelf, Antarctica. *Geophysics*, *57*(10), 1359–1372. doi: 10.1190/1.1443205

Begeman, C. B., Tulaczyk, S. M., & Fisher, A. T. (2017). Spatially Variable Geothermal Heat Flux in West Antarctica: Evidence and Implications. *Geophysical Research Letters*, *44*(19), 9823–9832. doi: 10.1002/2017GL075579

Bell, R. E., Ferraccioli, F., Creyts, T. T., Braaten, D., Corr, H., Das, I., ... Wolovick, M. (2011). Widespread Persistent Thickening of the East Antarctic Ice Sheet by Freezing from the Base. *Science*, *331*(6024), 1592–1595. doi: 10.1126/science.1200109

Bell, R. E., Studinger, M., Karner, G., Finn, C. A., & Blankenship, D. D. (2006). Identifying major sedimentary basins beneath the West Antarctic Ice Sheet from aeromagnetic data analysis. In D. K. Fütterer, D. Damaske, G. Kleinschmidt, H. Miller, & F. Tessensohn (Eds.), *Antarctica* (pp. 117–121). Berlin/Heidelberg: Springer-Verlag. doi: 10.1007/3-540-32934-X_13

Birch, F. (1984). Bedrock depth estimates from ground magnetometer profiles Werner deconvolution. *Ground Water*, *22*(4), 427–432. doi: 10.1111/j.1745-6584.1984.tb01413.x

Borg, S. G., Depaolo, D. J., & Smith, B. M. (1990). Isotopic structure and tectonics of the central Transantarctic mountains. *Journal of Geophysical Research*, *95*(B5), 6647. doi: 10.1029/JB095iB05p06647

Brancolini, G., Busetti, M., Marchetti, A., Santis, L. D., Zanolla, C., Cooper, A. K., ... Hinze, K. (1995). Descriptive text for the seismic stratigraphic atlas of the Ross Sea, Antarctica. In A. K. Cooper, P. F. Barker, & G. Brancolini (Eds.), *Geology and Seismic Stratigraphy of the Antarctic Margin* (Vol. 68, p. A271-A286). Washington, D. C.: American Geophysical Union. doi: 10.1002/9781118669013.app1

Burton-Johnson, A., Dziadek, R., & Martin, C. (2020). Geothermal heat flow in Antarctica: Current and future directions. *The Cryosphere Discussions*, 1–45. doi: 10.5194/tc-2020-59

Cheng, W., Hu, X. G., & Liu, L. T. (2021). Anisotropy Gradients in the Middle of the Ross Sea Embayment, West Antarctica: Evidence From QL Scattered Surface Waves. *Geophysical Research Letters*, *48*(6). doi: 10.1029/2020GL091232

Chiappini, M., Ferraccioli, F., Bozzo, E., & Damaske, D. (2002). Regional compilation and analysis of aeromagnetic anomalies for the Transantarctic Mountains–Ross Sea sector of the Antarctic. *Tectonophysics*, *347*(1-3), 121–137. doi: 10.1016/S0040-1951(01)00241-4

Christoffersen, P., Bougamont, M., Carter, S. P., Fricker, H. A., & Tulaczyk, S. (2014). Significant groundwater contribution to Antarctic ice streams hydrologic budget. *Geophysical Research Letters*, *41*(6), 2003–2010. doi: 10.1002/2014GL059250

Cochran, J. R., Burton, B., Frearson, N., & Tinto, K. (2014). IceBridge Scintrex CS-3 Cesium magnetometer L1B geolocated magnetic anomalies, version 2. [Line 403, 404]. *Boulder, Colorado USA. NASA National Snow and Ice Data Center Distributed Active Archive Center*. doi: 10.5067/OY7C2Y61YSYW

Coenen, J. J., Scherer, R. P., Baudoin, P., Warny, S., Castañeda, I. S., & Askin, R. (2019). Paleogene marine and terrestrial development of the West Antarctic Rift System. *Geophysical Research Letters*, *47*(3). doi: 10.1029/2019GL085281

Colleoni, F., De Santis, L., Montoli, E., Olivo, E., Sorlien, C. C., Bart, P. J., ... Prato, S. (2018). Past continental shelf evolution increased Antarctic ice sheet sensitivity to climatic conditions. *Scientific Reports*, *8*(1), 11323. doi: 10.1038/s41598-018-29718-7

Cooper, A. K., Barker, P. F., & Brancolini, G. (Eds.). (1995). *Geology and seismic stratigraphy of the Antarctic margin* (No. v. 68). Washington, D.C: AGU. doi: 10.1029/AR068

Corti, G., van Wijk, J., Cloetingh, S., & Morley, C. K. (2007). Tectonic inheritance and continental rift architecture: Numerical and analogue models of the East African Rift system. *Tectonics*, *26*(6), 1–13. doi: 10.1029/2006TC002086

Coulon, V., Bulthuis, K., Whitehouse, P. L., Sun, S., Haubner, K., Zipf, L., & Pattyn, F. (2021). Contrasting response of West and East Antarctic Ice Sheets to glacial isostatic adjustment. *Journal of Geophysical Research: Earth Surface*, *126*(7). doi: 10.1029/2020JF006003

Cox, S., Smith Lyttle, B., & 2019, S. G. A. G. (2019). SCAR GeoMAP dataset. *GNS Science*. doi: 10.21420/7SH7-6K05

Crary, A. P. (1961). Marine-sediment thickness in the eastern Ross Sea area, Antarctica. *Geological Society of America Bulletin*, *72*(5), 787. doi: 10.1130/0016-7606(1961)72[787:MTITER]2.0.CO;2

DeConto, R. M., & Pollard, D. (2003). A coupled climate–ice sheet modeling approach to the Early Cenozoic history of the Antarctic ice sheet. *Palaeogeography, Palaeoclimatology, Palaeoecology*, *198*(1-2), 39–52. doi: 10.1016/S0031-0182(03)00393-6

De Santis, L., Anderson, J. B., Brancolini, G., & Zayatz, I. (1995). Seismic record

of late Oligocene through Miocene glaciation on the central and eastern continental shelf of the Ross Sea. In A. K. Cooper, P. F. Barker, & G. Brancolini (Eds.), *Antarctic Research Series* (pp. 235–260). Washington, D. C.: American Geophysical Union. doi: 10.1029/AR068p0235

Drenth, B. J., Grauch, V., Turner, K. J., Rodriguez, B. D., Thompson, R. A., & Bauer, P. W. (2019). A shallow rift basin segmented in space and time: The southern San Luis Basin, Rio Grande rift, northern New Mexico, U.S.A. *Rocky Mountain Geology*, *54*(2), 97–131. doi: 10.24872/rmgjournal.54.2.97

Drewry, D. (1972). Subglacial morphology between the Transantarctic Mountains and the South Pole. In R. Adie (Ed.), *Antarctic Geology and Geophysics* (Vol. 1, pp. 693–703). Oslo: International Union of Geological Science. doi: 10.26153/tsw/2786

Ferraccioli, F., Bozzo, E., & Damaske, D. (2002). Aeromagnetic signatures over western Marie Byrd Land provide insight into magmatic arc basement, mafic magmatism and structure of the Eastern Ross Sea Rift flank. *Tectonophysics*, *347*, 139–165. doi: 10.1016/S0040-1951(01)00242-6

Finn, C. (2002). *Examples of the utility of magnetic anomaly data for geologic mapping* (Open-File Report No. 02-400). Denver, Colorado: USGS.

Fisher, A. T., Mankoff, K. D., Tulaczyk, S. M., Tyler, S. W., Foley, N., & and the WISSARD Science Team. (2015). High geothermal heat flux measured below the West Antarctic Ice Sheet. *Science Advances*, *1*, 1–9. doi: 10.1126/sciadv.1500093

Ford, A., & Barrett, P. J. (1975). *Basement rocks of the south-central Ross Sea, site 270, DSDP leg 28* (Tech. Rep.). College Station, TX, United States: Texas A & M University, Ocean Drilling Program. doi: 10.2973/dsdp.proc.28.130.1975

Frederick, B. C., Young, D. A., Blankenship, D. D., Richter, T. G., Kempf, S. D., Ferraccioli, F., & Siegert, M. J. (2016). Distribution of subglacial sediments across the Wilkes Subglacial Basin, East Antarctica. *Journal of Geophysical Research: Earth Surface*, *121*(4), 790–813. doi: 10.1002/2015JF003760

Fretwell, P., Pritchard, H. D., Vaughan, D. G., Bamber, J. L., Barrand, N. E., Bell, R. E., ... Zirizzotti, A. (2013). Bedmap2: Improved ice bed, surface and thickness datasets for Antarctica. *The Cryosphere*, *7*(1), 375–393. doi: 10.5194/tc-7-375-2013

Gooch, B. T., Young, D. A., & Blankenship, D. D. (2016). Potential groundwater and heterogeneous heat source contributions to ice sheet dynamics in critical submarine basins of East Antarctica. *Geochemistry, Geophysics, Geosystems*, *17*(2), 395–409. doi: 10.1002/2015GC006117

Goodge, J. W. (2020). Geological and tectonic evolution of the Transantarctic Mountains, from ancient craton to recent enigma. *Gondwana Research*, *80*, 50–122. doi: 10.1016/j.gr.2019.11.001

Granot, R., & Dyment, J. (2018). Late Cenozoic unification of East and West Antarctica. *Nature Communications*, *9*(1), 3189. doi: 10.1038/s41467-018-05270-w

Greischar, L. L., Bentley, C. R., & Whiting, L. R. (1992). An analysis of gravity measurements on the Ross Ice Shelf, Antarctica. In *Contributions to Antarctic Research III* (pp. 105–155). American Geophysical Union (AGU). doi: 10.1029/AR057p0105

Gustafson, C., Key, K., Siegfried, M., Winberry, J. P., Fricker, H. A., Venturelli, R., & Michaud, A. B. (2021). A deep and dynamic groundwater system beneath an Antarctic ice stream. In *AGU Fall Meeting 2021.* AGU.

Halberstadt, A. R. W., Simkins, L. M., Greenwood, S. L., & Anderson, J. B. (2016). Past ice-sheet behaviour: Retreat scenarios and changing controls in the Ross Sea, Antarctica. *The Cryosphere*, *10*(3), 1003–1020. doi: 10.5194/tc-10-1003-2016

Jolie, E., Scott, S., Faulds, J., Chambefort, I., Axelsson, G., Gutiérrez-Negrín, L. C.,

... Zemedkun, M. T. (2021). Geological controls on geothermal resources for power generation. *Nature Reviews Earth & Environment*, *2*(5), 324–339. doi: 10.1038/s43017-021-00154-y

Jordan, T. A., Riley, T. R., & Siddoway, C. S. (2020). The geological history and evolution of West Antarctica. *Nature Reviews Earth & Environment*, *1*, 117–133. doi: 10.1038/s43017-019-0013-6

Karner, G. D., Studinger, M., & Bell, R. E. (2005). Gravity anomalies of sedimentary basins and their mechanical implications: Application to the Ross Sea basins, West Antarctica. *Earth and Planetary Science Letters*, *235*, 577–596. doi: 10.1016/j.epsl.2005.04.016

Kingslake, J., Scherer, R. P., Albrecht, T., Coenen, J., Powell, R. D., Reese, R., ... Whitehouse, P. L. (2018). Extensive retreat and re-advance of the West Antarctic Ice Sheet during the Holocene. *Nature*, *558*(7710), 430–434. doi: 10.1038/s41586-018-0208-x

Ku, C. C., & Sharp, J. A. (1983). Werner deconvolution for automated magnetic interpretation and its refinement using Marquardt's inversion modeling. *Geophysics*, *48*(6), 754–774.

Kulhanek, D. K., Levy, R. H., Clowes, C. D., Prebble, J. G., Rodelli, D., Jovane, L., ... Naish, T. R. (2019). Revised chronostratigraphy of DSDP Site 270 and late Oligocene to early Miocene paleoecology of the Ross Sea sector of Antarctica. *Global and Planetary Change*, *178*, 46–64. doi: 10.1016/j.gloplacha.2019.04.002

Leckie, F. M. (1983). Late Oligocene-early Miocene glacial record of the Ross Sea, Antarctica: Evidence from DSDP Site 270. *Geology*, *11*, 578–582. doi: 10.1130/0091-7613(1983)11⟨578:LOMGRO⟩2.0.CO;2

Li, L., Aitken, A., Lindsay, M., & Kulessa, B. (2021). *Subglacial sedimentary basins focus key vulnerabilities of the Antarctic ice-sheet* (Preprint). In Review. doi: 10.21203/rs.3.rs-1117673/v1

Li, X., Zattin, M., & Olivetti, V. (2020). Apatite fission track signatures of the Ross Sea ice flows during the Last Glacial Maximum. *Geochemistry, Geophysics, Geosystems*, *21*(10), 1–21. doi: 10.1029/2019GC008749

Licht, K. J., Hennessy, A. J., & Welke, B. M. (2014). The U-Pb detrital zircon signature of West Antarctic ice stream tills in the Ross embayment, with implications for Last Glacial Maximum ice flow reconstructions. *Antarctic Science*, *26*(6), 687–697. doi: 10.1017/S0954102014000315

Lindeque, A., Gohl, K., Wobbe, F., & Uenzelmann-Neben, G. (2016). Preglacial to glacial sediment thickness grids for the Southern Pacific Margin of West Antarctica: Preglacial, transitional and full glacial isopach maps, West Antarctica. *Geochemistry, Geophysics, Geosystems*, *17*(10), 4276–4285. doi: 10.1002/2016GC006401

Lowry, D. P., Golledge, N. R., Bertler, N. A., Jones, R. S., McKay, R., & Stutz, J. (2020). Geologic controls on ice sheet sensitivity to deglacial climate forcing in the Ross Embayment, Antarctica. *Quaternary Science Advances*, *1*, 1–17. doi: 10.1016/j.qsa.2020.100002

Luyendyk, B., Sorlien, C. C., Wilson, D. S., Bartek, L. R., & Siddoway, C. S. (2001). Structural and tectonic evolution of the Ross Sea rift in the Cape Colbeck region, Eastern Ross Sea, Antarctica. *Tectonics*, *20*(6), 933–958. doi: 10.1029/2000TC001260

Luyendyk, B., Wilson, D. S., & Siddoway, C. S. (2003). Eastern margin of the Ross Sea Rift in western Marie Byrd Land, Antarctica: Crustal structure and tectonic development. *Geochemistry, Geophysics, Geosystems*, *4*(10), 1–25. doi: 10.1029/2002GC000462

Mooney, W. D., Laske, G., & Masters, T. G. (1998). CRUST 5.1: A global crustal model at 5° × 5°. *Journal of Geophysical Research: Solid Earth*, *103*(B1), 727–747. doi: 10.1029/97JB02122

Morlighem, M., Rignot, E., Binder, T., Blankenship, D., Drews, R., Eagles, G., ... Young, D. A. (2020). Deep glacial troughs and stabilizing ridges unveiled beneath the margins of the Antarctic ice sheet. *Nature Geoscience*, *13*(2), 132–137. doi: 10.1038/s41561-019-0510-8

Mortimer, N., Palin, J., Dunlap, W., & Hauff, F. (2011). Extent of the Ross Orogen in Antarctica: New data from DSDP 270 and Iselin Bank. *Antarctic Science*, *23*(3), 297–306. doi: 10.1017/S0954102010000969

Mouginot, J., Rignot, E., & Scheuchl, B. (2019). Continent-wide, interferometric SAR phase, mapping of Antarctic ice velocity. *Geophysical Research Letters*, *46*(16), 9710–9718. doi: 10.1029/2019GL083826

Müller, R. D., Gohl, K., Cande, S. C., Goncharov, A., & Golynsky, A. V. (2007). Eocene to Miocene geometry of the West Antarctic Rift System. *Australian Journal of Earth Sciences*, *54*(8), 1033–1045. doi: 10.1080/08120090701615691

Muto, A., Christianson, K., Horgan, H. J., Anandakrishnan, S., & Alley, R. B. (2013). Bathymetry and geological structures beneath the Ross Ice Shelf at the mouth of Whillans Ice Stream, West Antarctica, modeled from ground-based gravity measurements. *Journal of Geophysical Research: Solid Earth*, *118*(8), 4535–4546. doi: 10.1002/jgrb.50315

Neuhaus, S. U., Tulaczyk, S. M., Stansell, N. D., Coenen, J. J., Scherer, R. P., Mikucki, J. A., & Powell, R. D. (2021). Did Holocene climate changes drive West Antarctic grounding line retreat and readvance? *The Cryosphere*, *15*(10), 4655–4673. doi: 10.5194/tc-15-4655-2021

Paulsen, T., Encarnación, J., & Grunow, A. (2004). Structure and timing of transpressional deformation in the Shackleton Glacier area, Ross orogen, Antarctica. *Journal of the Geological Society*, *161*(6), 1027–1038. doi: 10.1144/0016-764903-040

Paxman, G. J. G., Jamieson, S. S., Hochmuth, K., Gohl, K., Bentley, M. J., Leitchenkov, G., & Ferraccioli, F. (2019). Reconstructions of Antarctic topography since the Eocene–Oligocene boundary. *Palaeogeography, Palaeoclimatology, Palaeoecology*, *535*, 109346. doi: 10.1016/j.palaeo.2019.109346

Pekar, S. F., DeConto, R. M., & Harwood, D. M. (2006). Resolving a late Oligocene conundrum: Deep-sea warming and Antarctic glaciation. *Palaeogeography, Palaeoclimatology, Palaeoecology*, *231*, 29–40. doi: 10.1016/j.palaeo.2005.07.024

Pérez, L. F., De Santis, L., McKay, R. M., Larter, R. D., Ash, J., Bart, P. J., ... 374 Scientists, I. O. D. P. E. (2021). Early and middle Miocene ice sheet dynamics in the Ross Sea: Results from integrated core-log-seismic interpretation. *GSA Bulletin*. doi: 10.1130/B35814.1

Ravier, E., & Buoncristiani, J.-F. (2018). Glaciohydrogeology. In *Past Glacial Environments* (pp. 431–466). Elsevier. doi: 10.1016/B978-0-08-100524-8.00013-0

Rignot, E., Jacobs, S., Mouginot, J., & Scheuchl, B. (2013). Ice-Shelf Melting Around Antarctica. *Science*, *341*(6143), 266–270. doi: 10.1126/science.1235798

Robertson, J. D., & Bentley, C. R. (1989). The Ross Ice Shelf: Glaciology and geophysics paper 3: Seismic studies on the grid western half of the Ross Ice Shelf: RIGGS I and RIGGS II. In C. R. Bentley & D. E. Hayes (Eds.), *Antarctic Research Series* (Vol. 42, pp. 55–86). Washington, D. C.: American Geophysical Union. doi: 10.1029/AR042p0055

Rooney, S. T., Blankenship, D. D., & Bentley, C. R. (1987). Seismic refraction measurements of crustal structure in West Antarctica. In G. D. Mckenzie (Ed.), *Geophysical Monograph Series* (pp. 1–7). Washington, D. C.: American Geophysical Union. doi: 10.1029/GM040p0001

Salvini, F., Brancolini, G., Busetti, M., Storti, F., Mazzarini, F., & Coren, F. (1997). Cenozoic geodynamics of the Ross Sea region, Antarctica: Crustal extension,

intraplate strike-slip faulting, and tectonic inheritance. *Journal of Geophysical Research: Solid Earth*, *102*(B11), 24669–24696. doi: 10.1029/97JB01643

Sauli, C., Sorlien, C., Busetti, M., De Santis, L., Geletti, R., Wardell, N., & Luyendyk, B. P. (2021). Neogene development of the Terror Rift, western Ross Sea, Antarctica. *Geochemistry, Geophysics, Geosystems*, *22*(3). doi: 10.1029/2020GC009076

Scambos, T., Haran, T., Fahnestock, M., Painter, T., & Bohlander, J. (2007). MODIS-based Mosaic of Antarctica (MOA) data sets: Continent-wide surface morphology and snow grain size. *Remote Sensing of Environment*, *111*(2-3), 242–257. doi: 10.1016/j.rse.2006.12.020

Shen, W., Wiens, D. A., Anandakrishnan, S., Aster, R. C., Gerstoft, P., Bromirski, P. D., ... Winberry, J. P. (2018). The crust and upper mantle structure of Central and West Antarctica from bayesian inversion of Rayleigh wave and receiver functions. *Journal of Geophysical Research: Solid Earth*, *123*(9), 7824–7849. doi: 10.1029/2017JB015346

Shen, W., Wiens, D. A., Lloyd, A. J., & Nyblade, A. A. (2020). A geothermal heat flux map of Antarctica empirically constrained by seismic structure. *Geophysical Research Letters*, *47*(14). doi: 10.1029/2020GL086955

Shen, W., Wiens, D. A., Stern, T., Anandakrishnan, S., Aster, R. C., Dalziel, I., ... Winberry, J. P. (2018). Seismic evidence for lithospheric foundering beneath the southern Transantarctic Mountains, Antarctica. *Geology*, *46*(1), 71–74. doi: 10.1130/G39555.1

Siddoway, C. S. (2008). Tectonics of the West Antarctic Rift System: New light on the history and dynamics of distributed intracontinental extension. In A. K. Cooper et al. (Eds.), *Antarctica: A Keystone in a Changing World.* Washington DC: The National Academies Press. doi: 10.3133/ofr20071047KP09

Siegert, M. J., Kulessa, B., Bougamont, M., Christoffersen, P., Key, K., Andersen, K. R., ... Smith, A. M. (2018). Antarctic subglacial groundwater: A concept paper on its measurement and potential influence on ice flow. *Geological Society, London, Special Publications*, *461*(1), 197–213. doi: 10.1144/SP461.8

Smith, W. H. F., & Wessel, P. (1990). Gridding with continuous curvature splines in tension. *GEOPHYSICS*, *55*(3), 293–305. doi: 10.1190/1.1442837

Sorlien, C. C., Luyendyk, B., Wilson, D. S., Decesari, R. C., Bartek, L. R., & Diebold, J. B. (2007). Oligocene development of the West Antarctic Ice Sheet recorded in eastern Ross Sea strata. *Geology*, *35*(5), 467. doi: 10.1130/G23387A.1

Stern, T. A., Davey, F. J., & Delisle, G. (1991). Lithospheric flexure induced by the load of the Ross Archipelago, southern Victoria land, Antarctica. In M. Thomson, A. Crame, & J. Thomson (Eds.), *Geological Evolution of Antarctica* (pp. 323–328). Cambridge, UK: Cambridge University Press.

Still, H., Campbell, A., & Hulbe, C. (2019). Mechanical analysis of pinning points in the Ross Ice Shelf, Antarctica. *Annals of Glaciology*, *60*(78), 32–41. doi: 10.1017/aog.2018.31

Studinger, M., Bell, R., Fitzgerald, P., & Buck, W. (2006). Crustal architecture of the Transantarctic Mountains between the Scott and Reedy Glacier region and South Pole from aerogeophysical data. *Earth and Planetary Science Letters*, *250*(1-2), 182–199. doi: 10.1016/j.epsl.2006.07.035

Studinger, M., Bell, R. E., Buck, W., Karner, G. D., & Blankenship, D. D. (2004). Sub-ice geology inland of the Transantarctic Mountains in light of new aerogeophysical data. *Earth and Planetary Science Letters*, *220*(3-4), 391–408. doi: 10.1016/S0012-821X(04)00066-4

ten Brink, U. S., Bannister, S., Beaudoin, B. C., & Stern, T. A. (1993). Geophysical investigations of the tectonic boundary between East and West Antarctica. *Science*, *261*(5117), 45–50. doi: 10.1126/science.261.5117.45

Tinto, K. J., Padman, L., Siddoway, C. S., Springer, S. R., Fricker, H. A., Das, I., ... Bell, R. E. (2019). Ross Ice Shelf response to climate driven by the tectonic imprint on seafloor bathymetry. *Nature Geoscience*, *12*(6), 441–449. doi: 10.1038/s41561-019-0370-2

Uieda, L., Tian, D., Leong, W. J., Jones, M., Schlitzer, W., Toney, L., ... Quinn, J. (2021). *PyGMT: A Python interface for the Generic Mapping Tools.* Zenodo. doi: 10.5281/zenodo.5607255

Venturelli, R. A., Siegfried, M. R., Roush, K. A., Li, W., Burnett, J., Zook, R., ... Rosenheim, B. E. (2020). Mid-Holocene grounding line retreat and readvance at Whillans Ice Stream, West Antarctica. *Geophysical Research Letters*, *47*(15). doi: 10.1029/2020GL088476

Werner, S. (1953). Interpretation of magnetic anomalies at sheet-like bodies. In *Sveriges Geologiska Undersok* (pp. 413–449). Stockholm Norstedt.

Wessel, P., Luis, J. F., Uieda, L., Scharroo, R., Wobbe, F., Smith, W. H. F., & Tian, D. (2019). The Generic Mapping Tools version 6. *Geochemistry, Geophysics, Geosystems*, *20*(11), 5556–5564. doi: 10.1029/2019GC008515

White-Gaynor, A. L., Nyblade, A. A., Aster, R. C., Wiens, D. A., Bromirski, P. D., Gerstoft, P., ... Anandakrishnan, S. (2019). Heterogeneous upper mantle structure beneath the Ross Sea Embayment and Marie Byrd Land, West Antarctica, revealed by P-wave tomography. *Earth and Planetary Science Letters*, *513*, 40–50. doi: 10.1016/j.epsl.2019.02.013

Whitehouse, P. L., Gomez, N., King, M. A., & Wiens, D. A. (2019). Solid Earth change and the evolution of the Antarctic Ice Sheet. *Nature Communications*, *10*(1), 503. doi: 10.1038/s41467-018-08068-y

Wilson, D. S., Jamieson, S. S., Barrett, P. J., Leitchenkov, G., Gohl, K., & Larter, R. D. (2012). Antarctic topography at the Eocene–Oligocene boundary. *Palaeogeography, Palaeoclimatology, Palaeoecology*, *335–336*, 24–34. doi: 10.1016/j.palaeo.2011.05.028

Wilson, D. S., & Luyendyk, B. (2009). West Antarctic paleotopography estimated at the Eocene-Oligocene climate transition. *Geophysical Research Letters*, *36*(16), L16302. doi: 10.1029/2009GL039297

Wilson, D. S., Pollard, D., DeConto, R. M., Jamieson, S. S., & Luyendyk, B. (2013). Initiation of the West Antarctic Ice Sheet and estimates of total Antarctic ice volume in the earliest Oligocene. *Geophysical Research Letters*, *40*(16), 4305–4309. doi: 10.1002/grl.50797

Zhou, Z., Wiens, D. A., Shen, W., Aster, R. C., Nyblade, A., & Wilson, T. J. (2022). Radial Anisotropy and Sediment Thickness of West and Central Antarctica Estimated From Rayleigh and Love Wave Velocities. *Journal of Geophysical Research: Solid Earth*, *127*(3). doi: 10.1029/2021JB022857

Geophysical Research Letters

Supporting Information for

Basement topography and sediment thickness beneath Antarctica's Ross Ice Shelf

M.D. Tankersley[1,2], H.J. Horgan[1], C.S. Siddoway[3], F. Caratori Tontini[2,4], K.J. Tinto[5]

[1]Antarctic Research Centre, Victoria University of Wellington, Wellington, New Zealand
[2]GNS Science, Lower Hutt, New Zealand
[3]Colorado College, Colorado Springs, CO, USA
[4]University of Genoa, Genoa, Italy
[5]Lamont-Doherty Earth Observatory, Columbia University, Palisades, NY, USA

Contents of this file

Introduction

This supplement provides additional information on the collection and processing of aeromagnetic line data (**Text S1**), the methodology of tying ROSETTA-Ice magnetic basement to ANTOSTRAT acoustic basement (Brancolini et al., 1995), through the use of Operation IceBridge(OIB) magnetic data (Cochran et al. 2014) (**Text S2 and S3**), the gridding, merging, and filtering of the resulting basement grid (**Text S4**), the calculation of sediment thickness and β-factors for the region (**Text S5**), and our quantification of uncertainties and comparison with points of previously measured sediment thickness (**Text S6**). Sediment thickness comparisons with past seismic surveys are included in **Table S1**. Also included are supplementary figures showing various additional Ross Ice Shelf grids (**Figure S1**), the Werner deconvolution solutions of OIB flight 403.3 (**Figure S2**), several selected ROSETTA-Ice flight lines with Werner deconvolution solutions (**Figure S3**), unfiltered basement solutions with flight line locations and individual Werner deconvolution solutions (**Figure S4**), and uncertainties applied to basement and sediment thickness results (**Figure S5**). Python code, within a Jupyter notebook, documents our workflow and figure creation, and is accessible here: https://zenodo.org/badge/latestdoi/470814953

Text S1. Magnetic data collection, processing, and Werner deconvolution

Both ROSETTA-Ice and OIB data sets were collected with a Scintrex CS3 Cesium magnetometer. Average flight speeds were 123 m/s and 93 m/s for OIB and ROSETTA-Ice respectively. Altitudes for the sections of OIB flight 403 used here average around 400 m above sea level, while ROSETTA-Ice altitude averaged at 750 m above ground level. OIB data were resampled from 20Hz to 1Hz to match the frequency of the ROSETTA-Ice data. Both datasets have been despiked, diurnally corrected, and had the International Geomagnetic Reference Field model removed. See Tinto et al. (2019) for more details of the ROSETTA-Ice survey and flight line locations. Due to variable flight elevations, both between and within the datasets, all magnetic data were upward-continued to 1000 m above sea level. To avoid artefacts of downwards continuing, any data with flight elevations above 1000 m were removed.

Here we use 2D Werner deconvolution (Werner, 1953, Ku & Sharp, 1983), applied to aeromagnetic line data, to image the shallowest magnetic signals in the crust. Assuming that the overlying sediments produce smaller magnetic anomalies than the crystalline basement, we treat the resulting solutions as a depth to the magnetic basement. During Werner deconvolution, moving and expanding windows are passed over the magnetic anomaly line data. Within each window, after linearly detrending the data, the source parameters of the anomalies are estimated with a least-squares approach, assuming the source bodies are infinite-depth dikes or contacts. The source parameters include position (distance along profile and depth), magnetic susceptibility, and source geometry (contact or dike). Solutions are considered valid between 1200 m and 20 km of upward continued flight elevation (approx. 200 m - 19 km bsl). Windows ranged from 500 m - 50 km, with a window shift increment of 1 km and an expansion of 1 km.

Due to passing over the data many times with varying window widths, Werner deconvolution produces a depth-scatter of solutions, which tend to cluster vertically beneath the true magnetic sources. Each of these solutions consists of location, depth, susceptibility (S), window width (W), and a simplified source geometry (dike or contact). For contact-type solutions, parameter S is the estimated magnetic susceptibility of the body, while for dike-type solutions, S is the product of susceptibility and dike width. During filtering (Text S2-3), a cut-off based on parameter S is used to remove shallow solutions. Since the value of parameter S for contact solutions are typically much smaller than for dike solutions (since they are not multiplied by dike width), only dike solutions have been considered here. To achieve a basement surface from this resulting depth-scatter of solutions, we have utilized parameter-based filtering and clustering, described in Text S2-3. This Werner deconvolution process was the same for both OIB and ROSETTA-Ice magnetics data. Werner deconvolution was performed in Geosoft's Oasis Montaj and subsequent processing of these results was performed in Python, and is included in a Jupyter notebook; https://zenodo.org/badge/latestdoi/470814953.

This magnetic basement approach has been used to map sedimentary basins throughout Antarctica, including the Ross Sea (Karner et al., 2005), western Marie Byrd Land (Bell et al., 2006), and Wilkes Subglacial Basin (Studinger et al., 2004; Frederick et al., 2016. Our approach is similar to past studies, but our proximity to well-constrained offshore seismic basement depths (Brancolini et al., 1995) allows us to develop the method further. Most studies display their results as 2D profiles with the depth-scatter of

solutions mentioned above, and simply use the tops of the clusters as the basement depth. By comparison with seismic basement, we have developed a reliable, automated method of 'draping' a surface over these depth-scattered solutions to produce a 3D surface. This process is described below.

Text S2. Tying magnetic basement to seismic basement

To validate this method and address uncertainty we perform Werner deconvolution for OIB magnetics data (Figure 1b, Cochran et al., 2014) over the Ross Sea. Here, ice-free conditions have permitted shipborne seismic surveys to image basement depths in the region. These have been compiled by the Antarctic Offshore Acoustic Stratigraphy project (ANTOSTRAT) (Brancolini et al., 1995) (Figure 1b). The basement was not imaged for the deeper portions of the basins and data coverage of actual basement reflectors, versus interpolation between basement reflectors, is not reported. Werner deconvolution (Text S1) produces a series of many solutions (black dots in Figures 2 & S2) at each window along the line.

To achieve a basement surface, instead of a depth-scatter of solutions, solutions were filtered based on Werner window width (W) and the product of magnetic susceptibility and body width (parameter S). Filtered solutions (black circles, scaled to parameter S in Figures 2 & S2) were then horizontally binned with variable bin sizes (parameter B) (vertical grey lines in Figures 2 & S2). Bins with a minimum count of solutions (parameter C) were retained, and the depth of the bin center was set to the 95^{th}-percentile depth of the solutions in the bin. This removed spurious shallow solutions, while effectively retaining the 'top' of the magnetic signal. These bin centers (orange crosses in Figures 2 & S2) were then interpolated, producing our model of magnetic basement depths (orange line in Figures 2 & S2). The above filtering techniques removed the solutions above the basement, and the clustering technique fitted a surface over the remaining points, which represents the top of the basement. This interpolated line allowed a direct comparison between ANTOSTRAT seismic basement and OIB magnetic basement.

We varied each of the four parameters (W, S, B, and C) with 21 different values and conducted the above procedures for all unique combinations of them on OIB line 403, segments 1 and 3, in the Ross Sea (location in Figure 1b). This resulted in 194,481 iterations, for each of which we calculated a mean absolute difference at points every 5km between ANTOSTRAT seismic basement and the resulting OIB magnetic basement. We found the parameter values which produced the closest match between OIB magnetic basement and ANTOSTRAT seismic basement, as shown in Figures 2 & S2. These resulting values were a maximum Werner deconvolution window width (parameter W) of 10 km, a minimum product of magnetic susceptibility and body width (parameter S) of 1.0, a horizontal bin width (parameter B) of 36 km, and a minimum number of solutions per bin (parameter C) of 6. The median absolute misfit between OIB and ANTOSTRAT basement for the two line-segments was 480 m (270 m for Line 403-1 (Figure 2), and 1060 m for Line 403-3 (Figure S2)). This equates to 11% of ANTOSTRAT depths. The close fit between the OIB magnetic basement and the ANTOSTRAT seismic basement both supports the validity of this method and gives us the parameters necessary to repeat this method for data over the RIS.

Text S3. Tying Ross Sea magnetic basement to Ross Ice Shelf magnetic basement

Having optimized our method to match OIB magnetic basement to ANTOSTRAT seismic basement in the Ross Sea (Text S2, Figures 2 & S2), we now optimize the method to match ROSETTA-Ice magnetic basement to OIB magnetic basement. This additional optimization is necessary due to differences in processing and survey design, including flight elevations, speed, aircraft, mounting equipment used, and frequency of recording. With the optimized parameters for OIB data (Text S2), we calculate magnetic basement for OIB flight 404 over the ice shelf. We treat this as the 'true' basement and update the filtering and clustering parameters (Text S1) to minimize the misfit between OIB basement and the resulting ROSETTA-Ice basement. This tuning was performed on ROSETTA-Ice lines 590 and 650, which were coincident with segments from OIB line 404 (location in Figures 1b & S4). Optimal parameters to match ROSETTA-Ice solutions to OIB basement are found to be W<26 km, S>1.2, B=36 km, and C>40, resulting in a median absolute misfit between OIB basement and ROSETTA-Ice solutions of 400 m (22% of OIB depth). With these parameters which best match ROSETTA magnetic basement to OIB magnetic basement, we performed the same procedure on all the ROSETTA-ice flight lines. A selection of these lines, and the two ties to OIB 404, are shown in Figure S3.

Text S4. Gridding, merging, and filtering

The above processes were performed on all ROSETTA-ice flight lines (white lines in Figure S4), including the N-S tie lines at ~55 km spacing. Where the tie lines crossed over the E-W flights lines, some resulting basement solutions (black dots in Figure S4) are nearby those from the crossing line. Since we are interested in the shallowest magnetic signals, we have retained only the shallowest solution with 8km cells across our region. Since bin widths (parameter B) were set to 36 km, the nearest solutions along individual lines were further apart than the 8km cell. The closest spacing of E-W flight lines was 10 km, so this process only affected solutions at the crossover between N-S and E-W lines. These points were then gridded with a 5 km cell size and a minimum curvature spline with a tension factor of 0.35 (Smith & Wessel, 1990) (Figure S4). This grid was then merged with a Ross Sea seismic basement grid. The Ross Sea grid, while mostly ANTOSTRAT data, was sourced from a regional compilation of sediment thicknesses (Lindeque et al., 2016, Wilson and Luyendyk 2009), we have subtracted from bathymetry depths (Morlighem et al. 2020) to achieve basement depths. Where the grids overlap near the ice shelf edge, we retain our RIS values. To aid in the merging at the overlaps, and to match RIS basement wavelengths to the characteristic basement wavelengths of ANTOSTRAT, we filtered the merged grid with an 80 km Gaussian filter (Figure 3a). This filtering was performed with a variety of wavelengths (20-120 km), where we found filters < 80 km didn't significantly alter the regional basement, while filters > 80 km excessively smoothed the basement topography.

Text S5. Sediment thickness and β-factor calculations

With the regional basement model (Figure 3a) including RIS magnetic basement and offshore seismic basement, we calculated sediment thickness (Figure 3b) by subtracting the grid from Bedmachine bathymetry depths (Figure1a & S1e, Morlighem et

al. 2020). Previous estimates of sediment thickness for the sub-RIS come from the extrapolation of gravity anomalies with bathymetry trends (Wilson and Luyendyk, 2009). These were included in the Lindeque et al. (2016) compilation (Figure S1d). Eocene-Oligocene boundary paleotopographic reconstructions (Wilson et al., 2012, Paxman et al., 2019) assumed this sediment estimate was post-Eocene and used it as their maximum sub-RIS sediment thickness, incorporated into their minimum surface reconstruction. The thickness of sediment affects onshore erosion estimates, surface raising due to deposition, and isostatic surface subsidence to due loading. For their maximum paleotopographic reconstructions, they used a thinner sediment model, with the same general trends (Wilson & Luyendyk, 2009). Figure S1 (c, d, & f) shows the comparison between the sediment thickness models. Figure S1f colorbar histogram shows the distribution, with our values having a mean thickness ~115m greater than the past model. Yet, along the Siple Coast, we show much greater discrepancies, up to 2 km thicker.

β-factor, the ratio of initial crustal thickness to final crustal thickness, is useful for quantifying the thinning of crust in extensional settings. We calculate a distribution of β-factors beneath the RIS by assuming a uniform initial crustal thickness and dividing it by current crustal thickness. We pick an initial crustal thickness of 38 km, which represents a global average for un-thinned plateau-type crust (Mooney et al., 1998), and has been used for the West Antarctic Rift System β-factor calculations (Müller et al., 2007). For the final (current) crustal thickness, we use a continent-wide Moho model from surface wave observations to define the bottom of the crust (An et al., 2015). For the top of the crust, we use our resulting RIS basement grid.

Text S6. Uncertainty and assumptions

We estimated a representative uncertainty for our basement model by examining the misfit of our modeled basement compared to offshore seismic basement depths (Brancolini et al., 1995). We did this by sampling our OIB magnetic basement estimate and the coincident ANTOSTRAT basement at 1 km intervals along lines 403-1 and 403-3 (Figures 2 and S2) and compared the values. The resulting absolute values of the differences don't exhibit a normal distribution; therefore, we use the median of the absolute misfit (+/-480m) as the basement model uncertainty. This equates to 22% of average basement depths for the sub-RIS. We performed a similar analysis between OIB magnetic basement and ROSETTA-Ice magnetic basement for coincident lines 590 and 650 (Figure S3 e & f). This resulted in a median absolute misfit of 400m. Tinto et al. (2019) report an uncertainty of 68m for their bathymetry model. Incorporating this with our basement model gives an uncertainty of 550m (37% of average thickness) for our sediment thickness results. Comparison with sub-RIS sediment thickness and distribution results from a variety of methods, including active source seismic surveys (Table S1 and references within), seismic radial anisotropy (Zhou et al., 2022), geophysical machine learning (Li et al. 2021), and magnetotelluric surveying (Gustafson et al. 2022, in review), all show general agreement with our results.

Our resulting basement grid is the depth to the shallowest magnetic signal. It is assumed that the crystalline basement in this region produces significantly larger magnetic anomalies compared to the overlying sediment fill. Note that in some

instances, such as igneous bodies intruded into sedimentary basin fill, Werner-determined solutions fall upon the crest of the intrusion, and the actual top of the crystalline basement could be at a deeper level. Intrusions of small lateral extent will have small widths, resulting in small values of parameter S (susceptibility x width) and therefore will be removed by our filter (Text S2). For larger intrusions into existing basins, (i.e. Ross Island and Minna Bluff (Cox et al., 2019)), the modeled magnetic basement surface will be shallower than the bottom of the sedimentary basin. While this underestimates sediment volume, it better characterizes the competency of the substrate from an ice dynamics perspective. This is similar to how extensive intrusions into basins would be imaged by seismic surveys as shallow basement. However, these extensive regions of late-Cretaceous-Cenozoic magmatism are not expected to be prevalent under the RIS (Andrews et al., 2021).

Name	Reference	Seismic sediment thickness (m)	Magnetic sediment thickness (m)	Absolute difference (m)
CIR	Rooney et al. (1987)	400	504	104
I10S	Robertson and Bentley (1989)	750+/-100	1624	874
J9DC	Greischar et al. (1992)	1350	771	579
BC	Robertson and Bentley (1989)	1900+/-400	1124	776
RI	Greischar et al. (1992)	850	807	43
C49	Crary (1961)	754	1162	408
LAS	Crary (1961)	1325	1820	495
Q13	Greischar et al. (1992)	255+/-145	744	489

Table S1. Previous seismic sediment thickness results for the Ross Ice Shelf. Stations names are labeled in Figure 3b. Magnetic sediment thickness column shows our sampled results at the location of each station. Comparing the seismic estimates with our sediment thickness at the eight stations gives a median absolute misfit of 480m.

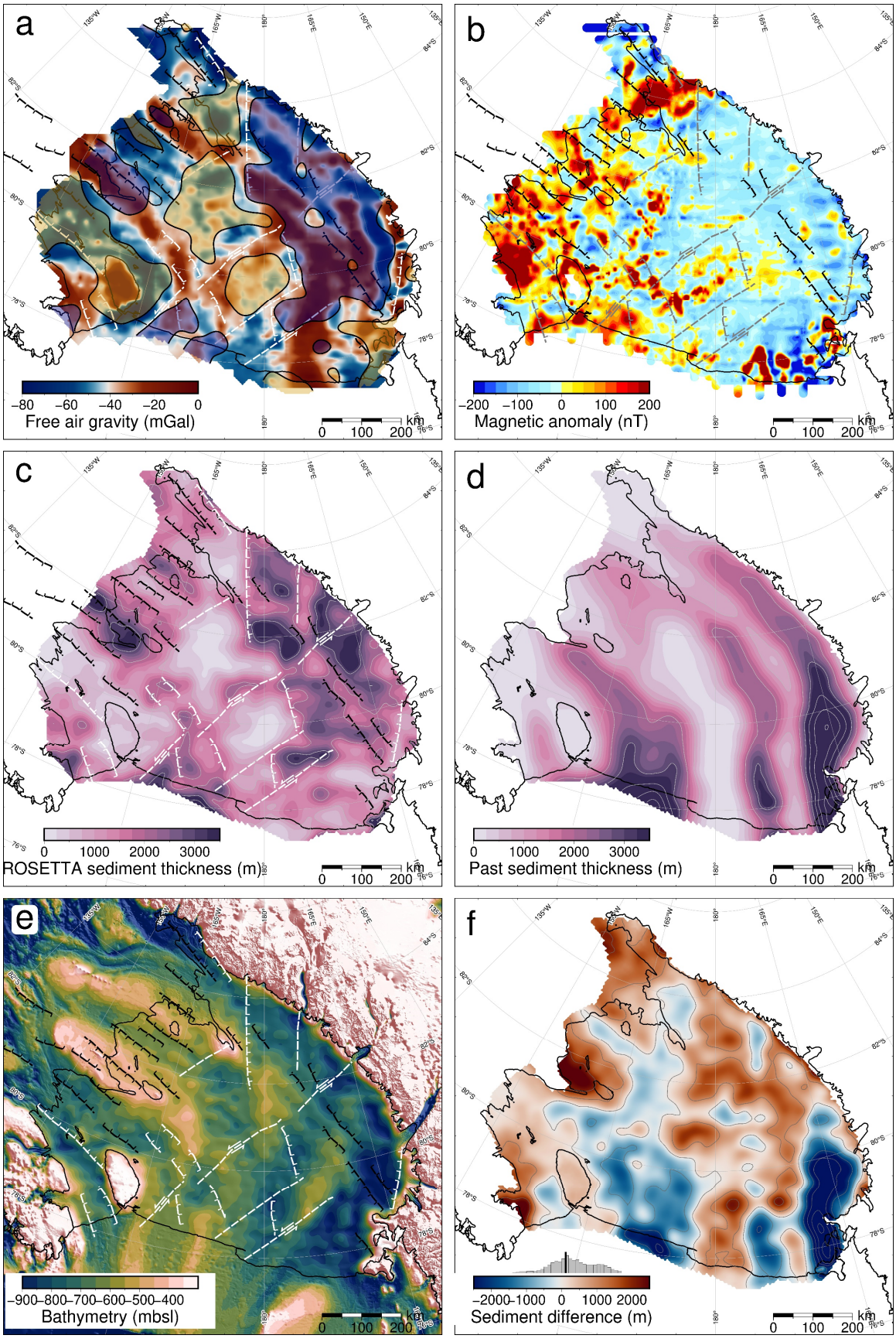
a
−80 −60 −40 −20 0
Free air gravity (mGal)
0 100 200 km
b
−200 −100 0 100 200
Magnetic anomaly (nT)
0 100 200 km
c
0 1000 2000 3000
ROSETTA sediment thickness (m)
0 100 200 km
d
0 1000 2000 3000
Past sediment thickness (m)
0 100 200 km
e
−900 −800 −700 −600 −500 −400
Bathymetry (mbsl)
0 100 200 km
f
−2000 −1000 0 1000 2000
Sediment difference (m)
0 100 200 km

Figure S1. (a) ROSETTA-Ice free air gravity (Tinto et al., 2019). Shaded yellow regions are shallow basement (< ~1600 mbsl), shaded blue regions are deep basement (> ~2600 mbsl). **(b)** ROSETTA-Ice airborne magnetic anomaly data (Tinto et al., 2019). **(c)** Sediment thickness from this study (same as Figure 3b), with 1 km contours. **(d)** Sediment thickness from a regional compilation (Text S5, Lindeque et al., 2016, Wilson & Luyendyk, 2009), with 1 km contours. **(e)** Bedmachine2 bathymetry (Morlighem et al., 2020), from which sediment thickness in (c) was calculated. **(f)** Difference between (c) and (d). Red signifies our results have more sediment, while blue signifies our results have less sediment. Histogram shows data distribution, with mean value (black) at 115m. Inferred faults in a),b),c), and e) same as Figure 4a. Grounding line and coastlines in black (Rignot et al., 2013). Projection is Antarctic Polar Stereographic: EPSG 3031.

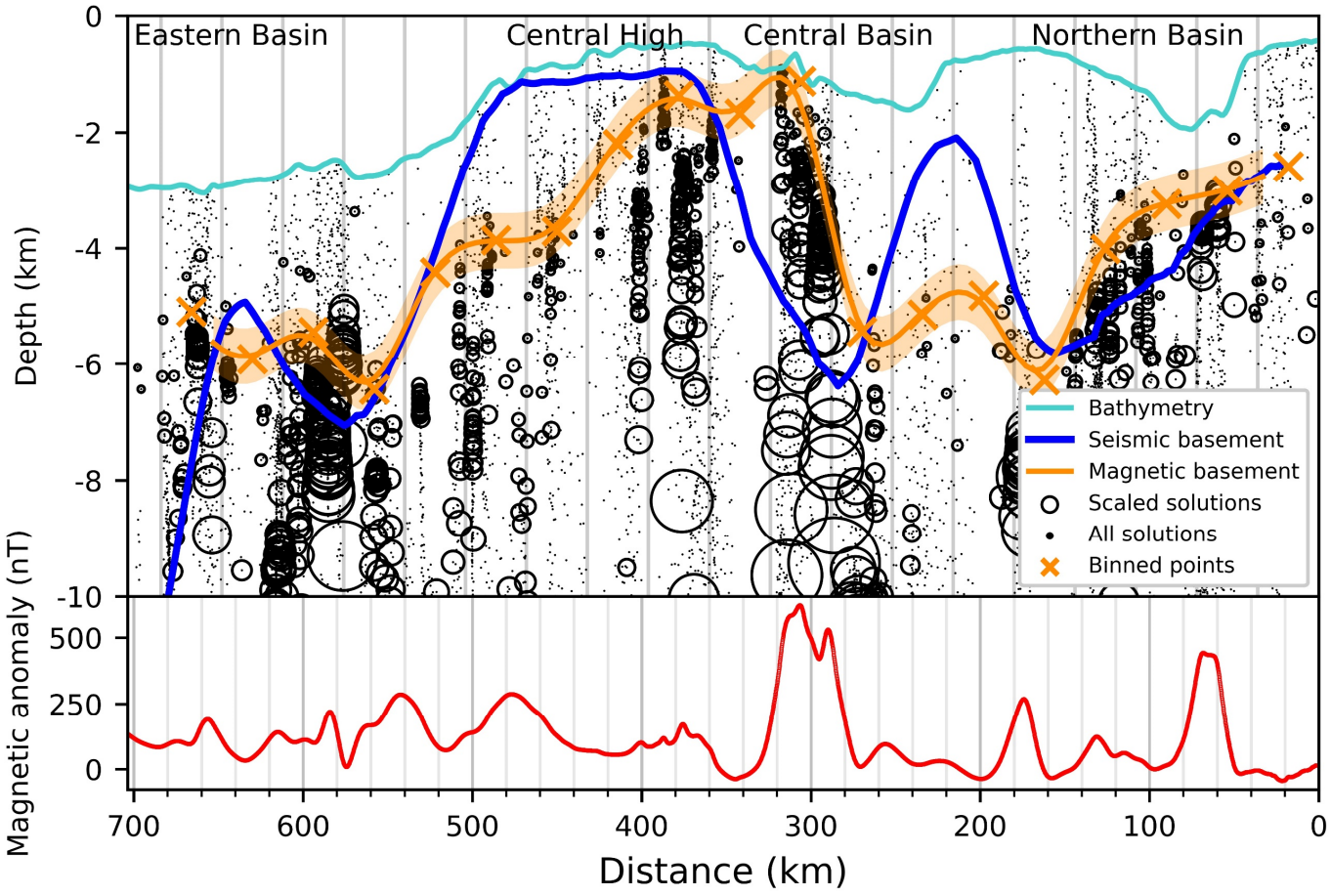

Figure S2. Ross Sea magnetic and seismic basement comparison. Operation IceBridge airborne magnetic data (lower panel) from segment 403-3 (Figure 1b). Small dots show Werner deconvolution solutions, which were filtered based on parameter S and W (Text S1) to produce black circles, which are scaled to parameter S. These circles were binned at a width equal to parameter B, shown by the vertical grey lines in the upper panel. Orange crosses show bin centers, which were fitted to a line to facilitate the comparison between the magnetic basement (orange line) and seismic basement (blue line). Orange band shows +/- 480m uncertainty for the basement model. Ross Sea basement features are labeled on top.

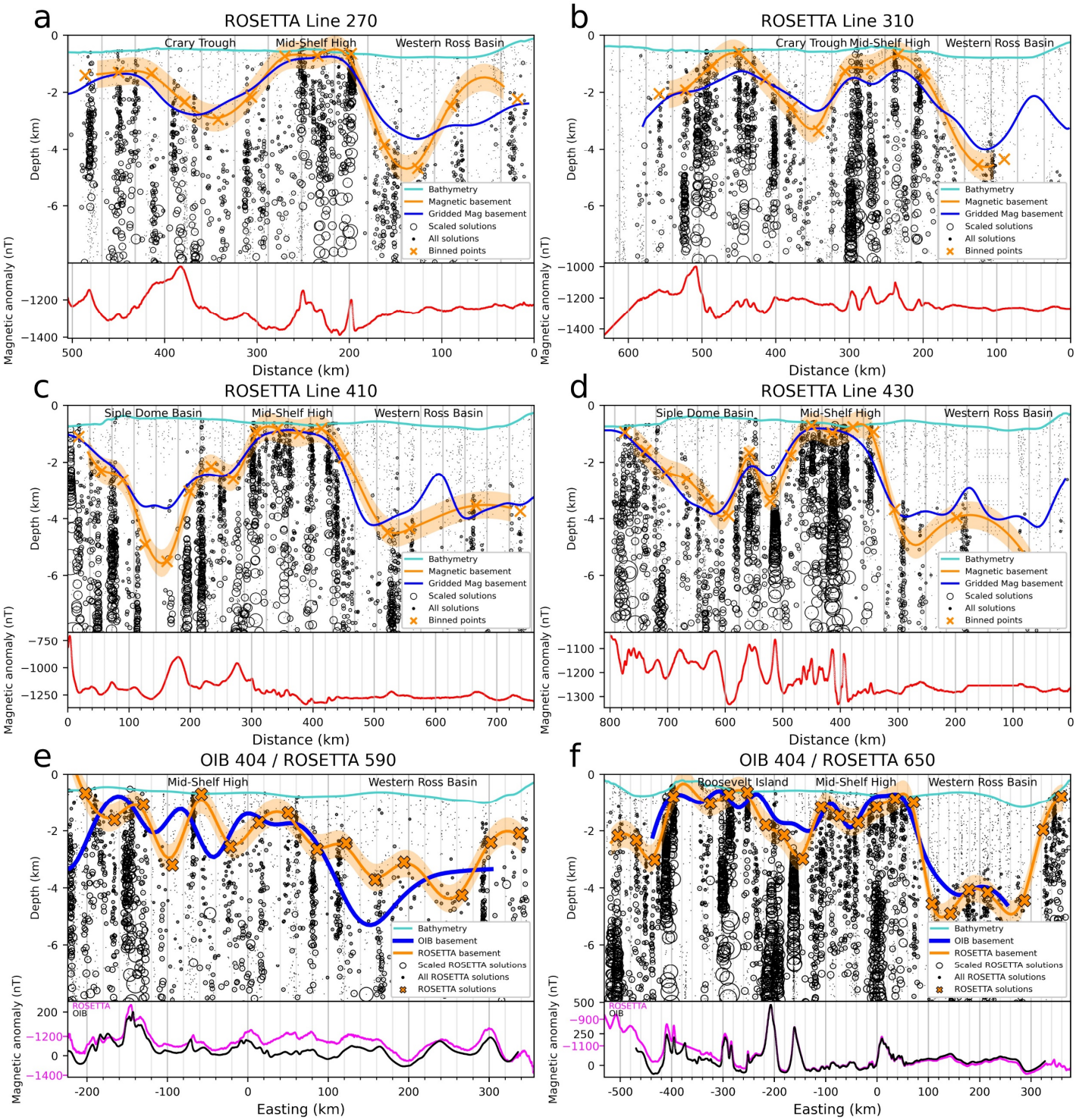

243 **Figure S3.** Werner deconvolution solutions for a selection of ROSETTA-Ice lines,
244 locations highlighted in Figure S4. Bathymetry from Bedmap2 (Fretwell et al., 2013). Dots,
245 circles, and vertical grey lines same as Figure S2. **a-d)** Comparison between magnetic
246 basement before and after filtering and gridding. Orange crosses are magnetic basement
247 solutions, shown as black dots inf Figure S4, and highlighted for these lines. Orange line
248 with uncertainty bounds is fitted to these solutions. Blue lines are magnetic basement

sampled from the grid of Figure 1a, after gridding and filtering. Red lines show ROSETTA-Ice magnetics data. **e-f)** Comparison between magnetic basement resulting from Werner deconvolution of coincident OIB and ROSETTA-Ice flight lines. Location is shown in Figures 1b and S4. These two lines were used to tie the ROSETTA-Ice survey to the OIB survey (Text S3). Blue lines are OIB magnetic basement results, orange crosses and fitted orange lines with uncertainty bands are ROSETTA-Ice magnetic basement. ROSETTA-Ice (pink) and OIB (black) magnetics data are shown in lower panels.

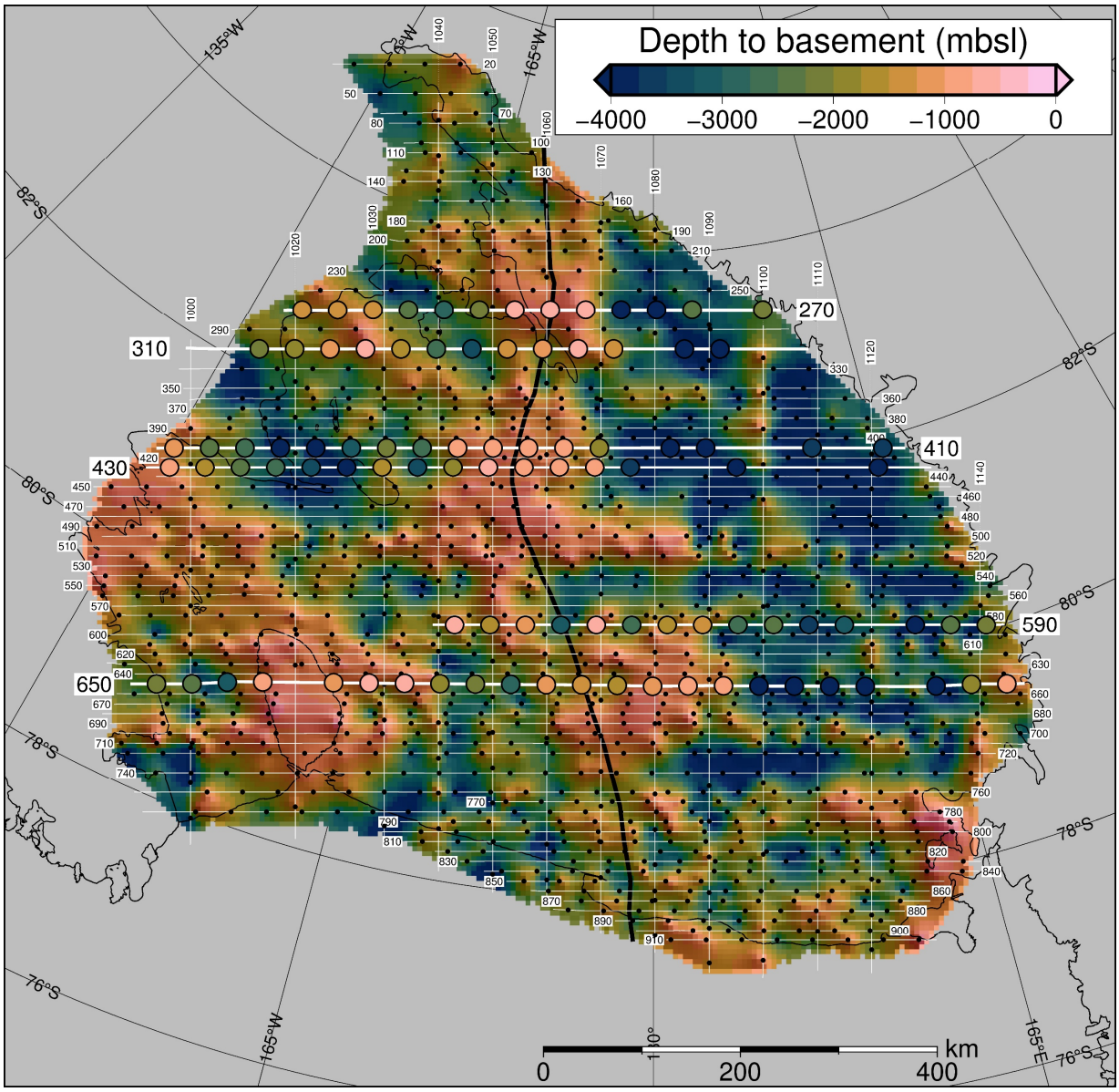

Figure S4. Unfiltered magnetic basement. Point solutions (black dots here, orange crosses in Figure S3) along ROSETTA-Ice flight lines (labeled) were gridded with a 5km cell size and a minimum curvature spline with a tension factor of 0.35. Figure S3 flight lines (bold white) and point solutions (colored circles) are shown. Black line through the Mid-Shelf High shows the East-West Antarctic divide used in colorbar histograms of Figures 3 and 4a. Grounding line and coastlines in black (Rignot et al., 2013).

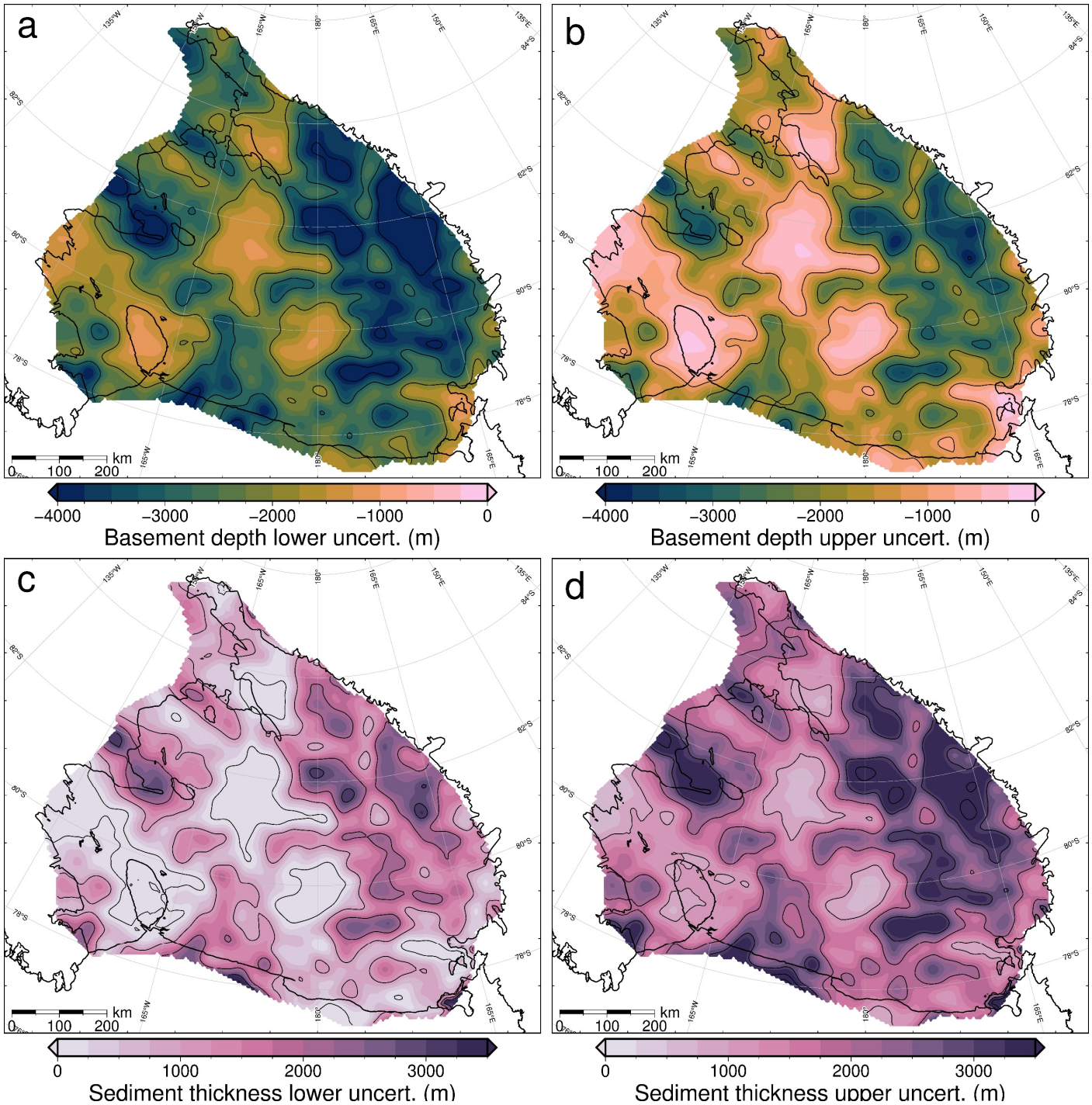

Figure S5. Upper and lower limits of uncertainty applied to **a-b)** magnetic basement and **c-d)** sediment thickness. See Text S6 for how these uncertainties were determined.